Progress In Electromagnetics Research B, Vol. 102, 115–130, 2023

Clutter and Ambiguity Reduction Using 3-Dimensional Side-Looking Synthetic Aperture Radar

Colin D. Kelly[1, *], Traian V. Dogaru[2], Kyle A. Gallagher[2], Calvin D. Le[2], Brian R. Phelan[2], and Ram M. Narayanan[1]

Abstract—Advancement in radar component technology has led to a reduction in the size, weight, and power consumption of radar systems. Experimental radar systems can now be integrated onto smaller, maneuverable platforms, such as small unmanned aerial vehicles (sUAVs). Integration onto rotor-based sUAVs enables data collection over novel synthetic apertures which can be optimized for different scenarios. The design, simulation, and experimentation of a light-weight, ultra-wideband synthetic aperture radar (SAR) is presented here that will be used for the detection of obscured surface targets. The approach outlined herein uses 3-dimensional (3-D) imagery to vertically resolve clutter from the target. A vertical-grid aperture is presented which yields vertical resolution. Point spread functions are derived for both linear and vertical-grid apertures. The analytical expressions are verified using simulations. Finally, experimental data is used to form 3-D imagery and demonstrate the importance of vertical resolution in the discrimination between scatterers above the ground, as well as clutter mitigation.

1. INTRODUCTION

Explosive remnants of war (ERWs) such as landmines, unexploded ordnances, and improvised explosive devices pose a constant threat in past areas of conflict throughout the world. The initial step in addressing this problem is to detect a large number of targets in the presence of clutter with high confidence. This task is further complicated by the variability of ERW emplacements. ERWs can be on the surface in the open, buried underground, or obscured by bushes and other natural clutter. Each of these scenarios requires a different approach for effective detection.

Surface targets can be found using side-looking synthetic aperture radar (SAR) in stripmap mode, in which the radar platform travels in a straight line and is pointing in a fixed direction. This allows for efficient scanning over a wide area, and is useful for unobscured surface targets which are easier to detect. However, detection becomes more difficult when targets are buried or obscured. When targets are buried, responses from the ground surface compete with that of the target. This is further exacerbated by the fact that the signal must propagate through a lossy medium. For these reasons, it is best to use a down-looking radar configuration so that a large amount of energy is coupled into the ground. Detection can be further improved by scanning the radar in a raster pattern to create 3-D imagery [1]. 3-D imaging distributes the clutter over a larger number of resolution cells so that the average clutter in each cell is reduced. This improves the ratio of the peak target response to the average clutter response, known as the signal-to-clutter ratio (SCR), and is used as a metric to assess the probability of detection. Another scenario that can occur includes obscured targets placed on the ground. Natural objects such as bushes create large clutter responses that can obscure target responses,

Received 9 May 2023, Accepted 25 July 2023, Scheduled 16 August 2023
* Corresponding author: Colin D. Kelly (cxk5246@psu.edu).
[1] The Department of Electrical Engineering and Computer Science, The Pennsylvania State University, University Park, PA 16802, USA. [2] The U.S. Army Combat Capabilities Development Command Army Research Laboratory, Adelphi, MD 20783, USA.

resulting in missed detections. In traditional stripmap SAR systems, which create 2-D images in the ground plane, both the reflected energy from the target and that of the foliage are projected onto the ground plane. This mixture of clutter and target energy greatly degrades detection performance. The solution presented in this paper seeks to follow the approach of down-looking radar systems by creating 3-D imagery to resolve the clutter and target into different resolution cells. Data collected over a vertical grid aperture enables 3-D imagery, but requires the maneuverability of a rotor-based sUAV.

SAR systems have traditionally been designed for larger platforms such as ground vehicles and fixed wing aircraft. These platforms could support large size, weight, and power (SWAP) radar systems. The sensing geometry for radars used for ERW detection can be grouped into three types of systems, down-looking, side-looking, and forward-looking. Down-looking systems typically consist of bumper mounted arrays that scan the road directly below the bumper while the ground vehicle cautiously drives forward [2–6]. This configuration has excellent coupling into the ground, making it suitable for ground penetrating radar (GPR) applications; however, a major drawback is the lack of standoff to dangerous targets. Forward-looking systems attempt to improve both the standoff and the scanning area coverage [7–12]. A large array is typically mounted on top of a ground vehicle and pointed forward. The real aperture provides resolution in the cross-range direction, while bandwidth provides resolution in the down-range direction. This configuration suffers from poor coupling of the radar waves into the ground. Side-looking systems are excellent for scanning wide areas of surface targets or shallow buried targets, but they also face a limitation in terms of power coupled into the ground [12–18].

Although the newest radio frequency (RF) technology has allowed for a reduction in system SWAP, a major component of the system, the antenna, is bounded in size by the longest wavelength of operation, and thus remains one of the largest subsystems. Good penetration of obstacles requires low operating frequencies (300 MHz to 2 GHz), which typically involve antennas proportional in size to the largest wavelength. All three SAR modalities discussed in the previous paragraph can be implemented on a single sUAV platform, and switching between sensing geometries can be achieved by a simple change in the antenna orientation. The ability to implement unconventional flight paths, including circular or 2-D raster scans, enable 3-D SAR image formation. For ERW detection, some UAV-mounted imaging radars documented in the literature are designed to detect buried targets and operate in down-looking mode [19–21], while other are configured as side-looking systems [22, 23], and are typically limited to shallow-buried or surface targets. The research presented in this paper seeks to demonstrate that 3-D radar imaging has the potential to significantly improve the detection of targets obscured by clutter. To obtain resolution in all three spatial directions, a 2-D synthetic aperture in side-looking mode is proposed.

This paper is organized as follows. Section 2 describes the imaging process and derives resolution and unambiguous range for various aperture geometries. A simple linear aperture is compared with a vertical grid aperture, demonstrating that the vertical grid aperture has resolution in the vertical dimension. Section 3 compares the derived point spread functions with simulations to validate the resolution expressions. Section 4 demonstrates the importance of vertical resolution in clutter reduction using experimental data. Section 5 discusses the results and proposes future work.

2. IMAGING THEORY

The radar system considered in this paper operates in stepped frequency mode. In this approach sinusoidal signals are transmitted at discrete frequencies f_l ranging from $f_c - \frac{B}{2}$ to $f_c + \frac{B}{2}$ (where B is the system's bandwidth and f_c is the center frequency), in Δf increments, and complex samples of the signal scattered by the scene under interrogation are collected by the receiver at each frequency step. To obtain a 2-D or 3-D image, the radar transmitter and receiver are moved across a synthetic aperture and the frequency stepping procedure is repeated for each spatial sample on this aperture. A monostatic radar system is considered in Sections 2 and 3, with propagation taking place in free-space. The coordinate system is chosen such that the image is centered about the origin, while the radar is placed at some range from the origin, as shown in Fig. 1.

The SAR system considered here operates with a fixed aperture length, and all aperture samples are used in focusing every image pixel/voxel, similar to a SAR system operating in spotlight mode. This is different from strip-map operation, where only a portion of the synthetic aperture is used in the

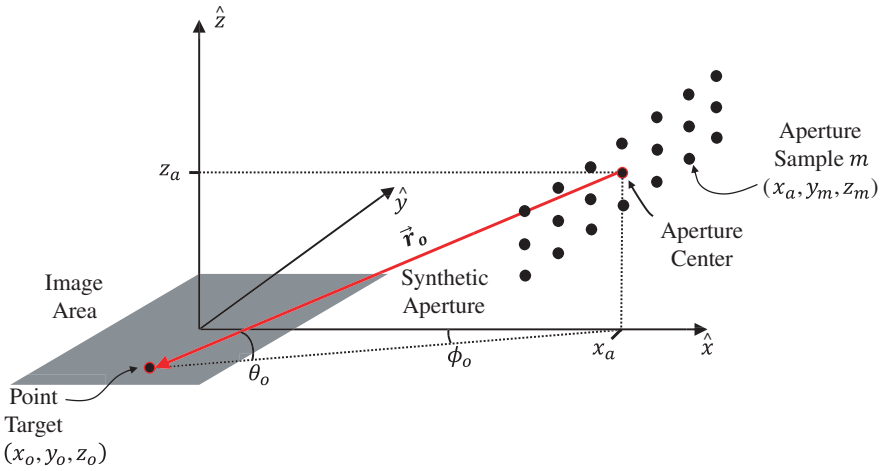

Figure 1. Aperture, image area, and point target, with angles defined to the aperture center.

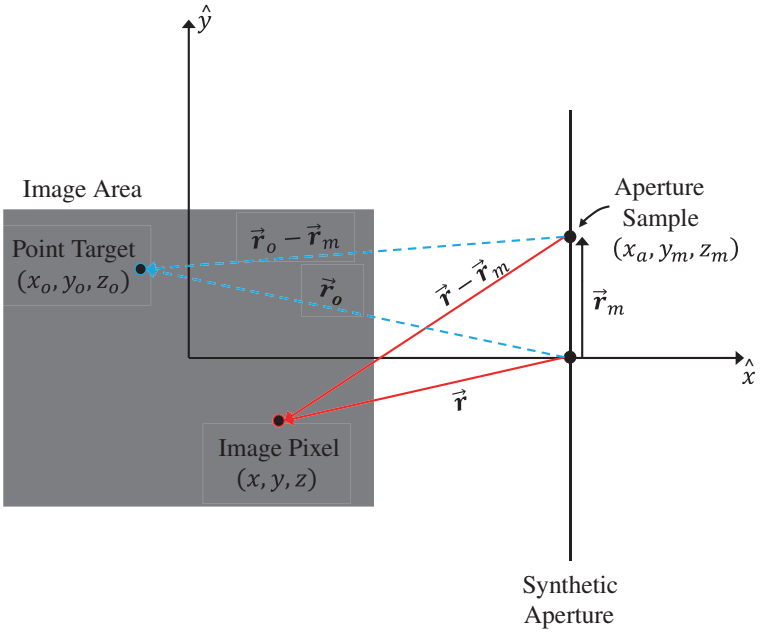

Figure 2. Top view of scene showing position vectors referenced to the center of the aperture.

image formation at a given pixel/voxel.

Position vectors are referenced to the center of the aperture, as shown in Fig. 2. A point target at the cartesian position (x_o, y_o, z_o) is characterized by the position vector $\vec{\mathbf{r}}_\mathbf{o} = [x_o - x_a \quad y_o \quad z_o - z_a]^T$. Furthermore, the length of $\vec{\mathbf{r}}_\mathbf{o}$ is denoted by $r_o = |\vec{\mathbf{r}}_\mathbf{o}|$.

The complex voltage signal received by the radar at aperture sample $\vec{\mathbf{r}}_\mathbf{m} = [0 \quad y_m \quad z_m - z_a]^T$ and frequency f_l depends on the transmit and receive antenna gains, the target scattering characteristics, and the radar-target propagation path [24]. Accounting for all these factors requires exact knowledge of each of these components, and modeling them requires full-wave, computationally intensive electromagnetic wave solvers. The first goal of this paper is to derive simplified analytic expressions for the point target response (PTR), and the point spread function (PSF) of the radar system with the purpose of understanding how the imaging performance is affected by geometric and frequency parameters. To this end, it is assumed that the antennas have omnidirectional patterns within the SAR system's integration angle and frequency-independent gains. It is also assumed that the scattering from the point target is

frequency- and angle-independent.

These simplifications leave us with the following expression for the PTR:

$$\mathrm{PTR}(\vec{\mathbf{r}}_\mathbf{o}, \vec{\mathbf{r}}_\mathbf{m}, f_l) = \frac{A}{k_l |\vec{\mathbf{r}}_\mathbf{o} - \vec{\mathbf{r}}_\mathbf{m}|^2} \exp\left(-j2k_l |\vec{\mathbf{r}}_\mathbf{o} - \vec{\mathbf{r}_\mathbf{m}}|\right), \tag{1}$$

where $k_l = \frac{2\pi f_l}{c}$ is the wavenumber characterizing the radar wave propagation, and A is a constant amplitude factor. Note that this form of the PTR is compatible with the radar equation [24], assuming that both antenna gains and the target reflectivity are frequency- and angle-independent.

The performance of the imaging system is typically characterized by the PSF, which is the system response to a point target. To form the radar image, the matched filter method is employed [24]. In this approach, the radar received signal is correlated with the PTR of a hypothetical point target at at a pixel/voxel located at $\vec{\mathbf{r}} = [x - x_a \quad y \quad z - z_a]^T$, to estimate the reflectivity at that pixel/voxel. In practice, only the conjugate of the phase factor in the PTR is used in the matched filter's transfer function. The PSF can be expressed as:

$$\begin{aligned}
\mathrm{PSF}(\vec{\mathbf{r}}, \vec{\mathbf{r}}_\mathbf{o}) &= \sum_{l=-\frac{L}{2}}^{\frac{L}{2}-1} \sum_{m=-\frac{M}{2}}^{\frac{M}{2}-1} \mathrm{PTR}(\vec{\mathbf{r}}_\mathbf{o}, \vec{\mathbf{r}}_\mathbf{m}, f_l) \exp\left(j \arg\{\mathrm{PTR}^*(\vec{\mathbf{r}}, \vec{\mathbf{r}}_\mathbf{m}, f_l)\}\right), \\
&= \sum_{l=-\frac{L}{2}}^{\frac{L}{2}-1} \sum_{m=-\frac{M}{2}}^{\frac{M}{2}-1} \frac{A}{k_l |\vec{\mathbf{r}}_\mathbf{o} - \vec{\mathbf{r}}_\mathbf{m}|^2} \exp\left(-j2k_l \left(|\vec{\mathbf{r}}_\mathbf{o} - \vec{\mathbf{r}}_\mathbf{m}| - |\vec{\mathbf{r}} - \vec{\mathbf{r}}_\mathbf{m}|\right)\right),
\end{aligned} \tag{2}$$

where L is the number of frequency steps, M the number of aperture samples, and $\arg\{\cdot\}$ the phase of the expression between the brackets.

In the most general case, the expression in Eq. (2) cannot be further simplified, so the only way to rigorously determine the imaging system's resolution would require numeric simulations. However, analytic expressions for the resolution can be established if certain simplifying assumptions and approximations are made. In Section 3, we assess the errors introduced by these approximations by comparing the PSF obtained via direct implementation of the formula in Eq. (2) with the analytic expressions obtained in Sections 2.1 and 2.2.

First, the amplitude factor $\frac{A}{k_l |\vec{\mathbf{r}}_\mathbf{o} - \vec{\mathbf{r}}_\mathbf{m}|^2}$ is dropped from the double sum in Eq. (2). Next, the aperture vector length, $|\vec{\mathbf{r}}_\mathbf{m}|$, is assumed to be much smaller than the pixel and target vector lengths, $|\vec{\mathbf{r}}|$ and $|\vec{\mathbf{r}}_\mathbf{o}|$, respectively, which is equivalent to assuming a narrow aperture. Making use of this assumption, the range to a pixel from aperture sample m is approximated:

$$|\vec{\mathbf{r}} - \vec{\mathbf{r}}_\mathbf{m}| \approx r - \frac{y y_m + z z_m}{r}. \tag{3}$$

A similar approximation can be established for the $|\vec{\mathbf{r}}_\mathbf{o} - \vec{\mathbf{r}}_\mathbf{m}|$ range to obtain:

$$|\vec{\mathbf{r}}_\mathbf{o} - \vec{\mathbf{r}}_\mathbf{m}| - |\vec{\mathbf{r}} - \vec{\mathbf{r}}_\mathbf{m}| \approx r_o - r - \frac{y_o y_m + z_o z_m}{r_o} + \frac{y y_m + z z_m}{r}. \tag{4}$$

Furthermore, the approximation $r \approx r_o$ is applied in the denominators in Eq. (4). This assumption implies that we are investigating a pixel relatively close to the point target. Finally, it is assumed that $k_l \approx k_c$ in the exponentials concerning y and z. This implies a narrow bandwidth. These assumptions allow the double sum to be separated. Consequently, the PSF is approximated by the following expression:

$$\mathrm{PSF}(\vec{\mathbf{r}}, \vec{\mathbf{r}}_\mathbf{o}) = \sum_{l=-\frac{L}{2}}^{\frac{L}{2}-1} \exp\left(-j2k_l \left(r_o - r\right)\right) \sum_{m=-\frac{M}{2}}^{\frac{M}{2}-1} \exp\left(-j2k_c \frac{y_m (y - y_o)}{r_o}\right) \exp\left(-j2k_c \frac{z_m (z - z_o)}{r_o}\right). \tag{5}$$

In the following two subsections, a linear horizontal aperture and a grid-like 2-D vertical aperture are considered.

2.1. Linear Aperture

A linear synthetic aperture oriented along the y-axis is considered first, as shown in Fig. 1. The aperture is centered at $y = 0\,\mathrm{m}$ and sampled at coordinates y_m in Δy increments, with $m = -\frac{M}{2}, \ldots, \frac{M}{2} - 1$, while x_a and z_a are the other two (fixed) aperture sample coordinates. The image is created in the ground plane ($z = 0\,\mathrm{m}$) and we consider a target placed in the ground plane as well ($z_o = 0\,\mathrm{m}$).

For that configuration, the resulting PSF is:

$$\mathrm{PSF}(\vec{\mathbf{r}}, \vec{\mathbf{r}}_\mathbf{o}) = \sum_{l=-\frac{L}{2}}^{\frac{L}{2}-1} \exp\left(-j2k_l\left(r_o - r\right)\right) \sum_{m=-\frac{M}{2}}^{\frac{M}{2}-1} \exp\left(-j2k_c \frac{y_m(y - y_o)}{r_o}\right). \tag{6}$$

Each of the separate factors can be computed based on the geometrical series sum formula:

$$\sum_{p=-\frac{P}{2}}^{\frac{P}{2}-1} \exp\left(jpu\right) = \exp(j\psi) \frac{\sin\left(\dfrac{Pu}{2}\right)}{\sin\left(\dfrac{u}{2}\right)}, \tag{7}$$

where ψ is a constant phase that can be neglected in the final expression of the PSF magnitude.

The final result for the PSF is:

$$\mathrm{PSF}(\vec{\mathbf{r}}, \vec{\mathbf{r}}_\mathbf{o}) \approx \frac{\sin\left(\dfrac{2\pi B}{c}(r_o - r)\right)}{\sin\left(\dfrac{2\pi \Delta f}{c}(r_o - r)\right)} \times \frac{\sin\left(\dfrac{2\pi A_y}{r_o \lambda_c}(y - y_o)\right)}{\sin\left(\dfrac{2\pi \Delta y}{r_o \lambda_c}(y - y_o)\right)}, \tag{8}$$

where $B = L\Delta f$ is the system bandwidth, and $A_y = M\Delta y$ is the aperture length.

The two sine ratios in the previous equation are called aliased sinc functions [24]. To determine the resolution in each direction, we evaluate the mainlobe width of each digital sinc factor. According to the Rayleigh Criterion, the system's resolution is taken as half the mainlobe width in each direction [24]. Note that the first sinc contains radial terms, whereas the second depends on the y coordinates only (cross-range). The radial terms can be expanded in terms of x, y, and z using the following relations:

$$\begin{aligned} r &= x\cos\theta\cos\phi + y\cos\theta\sin\phi + z\sin\theta \\ r_o &= x_o\cos\theta_o\cos\phi_o + y_o\cos\theta_o\sin\phi_o + z_o\sin\theta_o \end{aligned} \tag{9}$$

Since $z = 0$ and $z_o = 0$, those terms are removed. Again, we assume that the pixel is close to the target, so that $\theta \approx \theta_o$ and $\phi \approx \phi_o$. The range vector difference is given by

$$\begin{aligned} r_o - r \;&\approx\; (x_o - x)\cos\theta_o\cos\phi_o + (y_o - y)\cos\theta_o\sin\phi_o \\ &= \frac{(x_o - x)(x_o - x_a)}{r_o} + \frac{(y - y_o)y_o}{r_o}. \end{aligned} \tag{10}$$

This shows that the first sinc determines resolution in both the x and y directions. These resolutions are related to that in $\vec{\mathbf{r}}$ by

$$\begin{aligned} \delta_x &= \delta_r \frac{r_o}{|x_o - x_a|} \\ \delta_y &= \frac{\delta_r r_o}{|y_o|}, \end{aligned} \tag{11}$$

where $\delta_r = \frac{c}{2B}$ and $r_o = \sqrt{(x_o - x_a)^2 + y_o^2 + (z_o - z_a)^2}$. Since both sinc expressions contain the y variable, the resolution in this direction is taken as the minimum of the two y-directed expressions. The final expressions for down-range and cross-range resolutions are, respectively:

$$\begin{aligned} \delta_x &= \frac{c}{2B}\frac{r_o}{|x_o - x_a|} \\ \delta_y &= \min\left(\frac{\lambda_c r_o}{2A_y}, \frac{c}{2B}\frac{r_o}{|y_o|}\right) \end{aligned} \tag{12}$$

These formulas indicate that targets placed further away from the image center in cross-range (increased y) exhibit degraded resolution in both down-range and cross-range directions. Additionally, image pixels placed further away from the radar in down-range (increased $x_a - x_o$) display worse resolution in cross-range but improved resolution in down-range.

The nulls of the denominators in Eq. (8) determine the locations of the image grating lobes. It is of interest to determine the distances from the mainlobe to the first grating lobe in the two directions (down-range and cross-range), which dictate the unambiguous image size. These are:

$$\begin{aligned} D_x^u &= \frac{c}{2\Delta f}\frac{r_o}{|x_o - x_a|} \\ D_y^u &= \min\left(\frac{\lambda_c r_o}{2\Delta y}, \frac{c}{2\Delta f}\frac{r_o}{|y_o|}\right). \end{aligned} \tag{13}$$

The analysis performed so far indicates the parameters in the system design that can be used to set the resolution and unambiguous ranges. Thus, for improved down-range resolution (small δ_x) a wide frequency bandwidth is necessary, as well as a small slant angle. To improve the cross-range resolution (decrease δ_y), a wide aperture, higher frequencies, and a short radar-image range should be used. The unambiguous ranges can be increased by reducing the sampling step size in frequency and aperture position, respectively. Cross-range resolution is dependent on squint angle, which is defined as the angle between antenna boresight and a vector perpendicular to the direction-of-travel. To improve resolution (decrease δ_y) under this condition, a wide aperture, higher frequencies, and a short radar-image range should be used. At large squint angles, cross-range resolution is improved by increasing signal bandwidth. This paper is interested in geometries with a small squint angle. Unambiguous range in down-range and cross-range is increased by reducing the sampling step size in frequency and aperture position, respectively.

It should be noted that the radar sensing configurations characteristic to ERW detection applications typically do not satisfy the narrow bandwidth and narrow aperture assumptions made in this section. Particularly, the experimental setup described in Section 4 of this paper involves a wide frequency band and a wide angle aperture. Nevertheless, the formulas established in this section to estimate the resolutions and unambiguous ranges are still useful in characterizing the imaging system performance. The validity of these formulas is checked against rigorous numerical simulations in Section 3.

When the target is not located in the ground plane (as assumed in the derivations in this subsection), its ground plane image becomes defocused, and the resolution typically degrades. This is particularly true in SAR systems operating at near ranges, such that the height of scatterers in the scene is on the order of the target range. Additionally, the target may not appear at the correct x and y coordinates in the ground plane image. To alleviate these problems, a 3-D imaging system is proposed, as described in Subsection 2.2.

2.2. Vertical Grid Aperture

Next, the grid-like vertical aperture, shown in Fig. 3, is considered. The grid is centered at $(x_a, 0, z_a)$ and treated as a set of N horizontal apertures, each containing M samples. Samples are uniformly spaced in y and z directions, with a spacing of Δy and Δz, respectively. The image is now created in a 3-D cube, and the target is placed at an arbitrary position within the cube.

The analysis begins with Eq. (6); however, there are now N linear apertures, so a summation is added over $n \in \left\{-\frac{N}{2}, \ldots, \frac{N}{2} - 1\right\}$. Aperture sample height is now a function of z_n and the resulting PSF contains three separable summations:

$$\begin{aligned} \mathrm{PSF}(\vec{\mathbf{r}}, \vec{\mathbf{r}}_\mathbf{o}) \;=\; & \sum_{l=-\frac{L}{2}}^{\frac{L}{2}-1} \exp\left(-j2k_l\left(r_o - r\right)\right) \sum_{m=-\frac{M}{2}}^{\frac{M}{2}-1} \exp\left(-j2k_c\frac{y_m(y-y_o)}{r_o}\right) \\ & \sum_{n=-\frac{N}{2}}^{\frac{N}{2}-1} \exp\left(-j2k_c\frac{z_n(z-z_o)}{r_o}\right). \end{aligned} \tag{14}$$

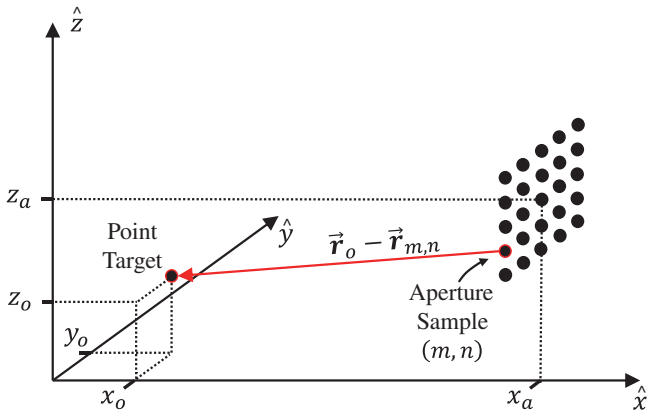

Figure 3. Grid aperture samples.

The resulting approximate PSF is:

$$\mathrm{PSF}(\vec{\mathbf{r}}, \vec{\mathbf{r}}_\mathbf{o}) \approx \frac{\sin\left(\frac{2\pi B}{c}(r_o - r)\right)}{\sin\left(\frac{2\pi \Delta f}{c}(r_o - r)\right)} \times \frac{\sin\left(\frac{2\pi A_y}{r_o \lambda_c}(y - y_o)\right)}{\sin\left(\frac{2\pi \Delta y}{r_o \lambda_c}(y - y_o)\right)} \times \frac{\sin\left(\frac{2\pi A_z}{r_o \lambda_c}(z - z_o)\right)}{\sin\left(\frac{2\pi \Delta z}{r_o \lambda_c}(z - z_o)\right)} \tag{15}$$

The first sinc factor is a radial expression that contributes to resolution in each dimension, while the second and third factors contribute to resolution in y and z directions only, respectively. Resolution in each direction is determined by the minimum between the the contributing expressions.

$$\begin{aligned} \delta_x &= \frac{c}{2B} \frac{r_o}{|x_o - x_a|} \\ \delta_y &= \min\left(\frac{\lambda_c r_o}{2A_y}, \frac{c}{2B}\frac{r_o}{|y_o|}\right) \\ \delta_z &= \min\left(\frac{\lambda_c r_o}{2A_z}, \frac{c}{2B}\frac{r_o}{|z_o - z_a|}\right) \end{aligned} \tag{16}$$

Again, it is assumed that the squint angle, ϕ_s, is small. Typically, the radial component of the resolution, relating to the bandwidth, determines the down-range resolution, δ_x. In the y and z dimensions, the size of the aperture in that dimension determines resolution. These expressions demonstrate the dependence that resolution has on target position. The resolution in the down-range dimension is degraded as $|y_o|$ increases but is improved as the height of the target approaches z_a. The cross-range resolution of the target improves as the down-range position of the target approaches x_a and as the height of the target approaches z_a. Vertical resolution improves as the down-range position of the target approaches x_a and degrades as $|y_o|$ increases.

The grating lobe separation in each dimension is

$$\begin{aligned} D_x^u &= \frac{c}{2\Delta f} \frac{r_o}{|x_o - x_a|} \\ D_y^u &= \min\left(\frac{\lambda_c r_o}{2\Delta y}, \frac{c}{2B}\frac{r_o}{|y_o|}\right) \\ D_z^u &= \min\left(\frac{\lambda_c r_o}{2\Delta z}, \frac{c}{2B}\frac{r_o}{|z_o - z_a|}\right) \end{aligned} \tag{17}$$

The resolution terms in the x and y directions match those of Section 2.1 exactly. Resolution in the vertical dimension is improved using a large vertical aperture, A_z. With this added capability, targets can be accurately located within a 3-D image. Additionally, this allows the spreading of the clutter energy across a larger number of voxels, lowering the average amount of clutter in each pixel/voxel and improving target detectability.

3. SIMULATIONS

The expressions derived in Section 2 are verified herein using simulated PSFs. Validating the resolution formulas established in Section 2 is the primary interest, so any amplitude factors are ignored, such that all PSFs are normalized to their peak magnitudes. The matched filter method is used to form the imagery. The matched filter method from Eq. (2). is used to form simulated PSFs. The analytical PSFs derived in Section 2 are compared with the simulated PSFs to determine their validity. A target is simulated at $(x_o, y_o, z_o) = (-1, 0.5, 1.5)\,\mathrm{m}$ using the two types of apertures discussed in Section 2. This position is used to demonstrate that the expressions derived in Section 2 are valid at any arbitrary target position. As in the previous derivations, the aperture is set at a fixed across-track position. In this simulation, the across-track position is $x_a = 4\,\mathrm{m}$. The along-track dimension is y and the vertical dimension is z. In both simulations, the aperture has a horizontal extent of $D_y = 5\,\mathrm{m}$. The spacing between samples is $\Delta y = 0.006\,\mathrm{m}$. For the grid aperture, the vertical extent is $D_z = 1.4\,\mathrm{m}$, and the vertical spacing between samples is $\Delta z = 0.05\,\mathrm{m}$. The frequency band of the simulation spans from 2.2 GHz to 3.7 GHz, with a 1.5 MHz sampling step size.

The simulated apertures and point target are shown in Fig. 4. First, the linear aperture is considered.

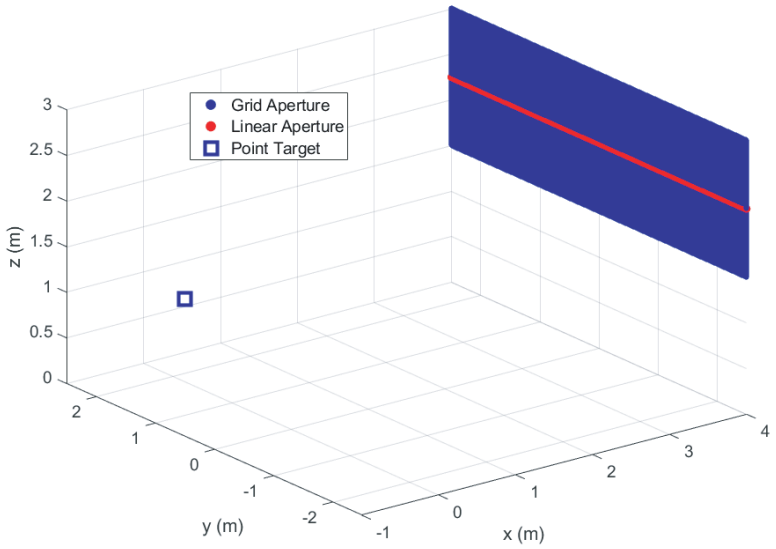

Figure 4. Linear aperture and the target.

Typically, images formed using a linear aperture are created in the ground plane. The images in Fig. 5 are formed in two horizontal planes. A hanning window was applied in both range and aperture dimensions of these images for sidelobe control. The first image is formed at the height of the target (1.5 m), and the second image is formed in the ground plane. Since there is no vertical resolution, the target response strength is the same at both heights. The image created at the target height shows the target at the correct (x, y) position and maintains the resolution dictated by the frequency band and aperture length. The target response in the ground plane is shifted in across-track position.

The shift in across-track position is due to the nature of the vertical ambiguity of the radar image. Resolution is achieved on a sphere whose radius is the range from the center of the aperture to the target. Due to the lack of vertical resolution, a circle of ambiguity appears in the vertical plane perpendicular to the antenna's direction of travel. This circle occurs at the cross-range position of the target. Vertical resolution resolves the ambiguity along this circle. The implication of a lack of vertical resolution is that out-of-plane scatterers and clutter will project onto the image plane, degrading the target detection performance [25].

The expected resolution in each dimension at the height of the target is $\delta_x = 0.101\,\mathrm{m}$ and

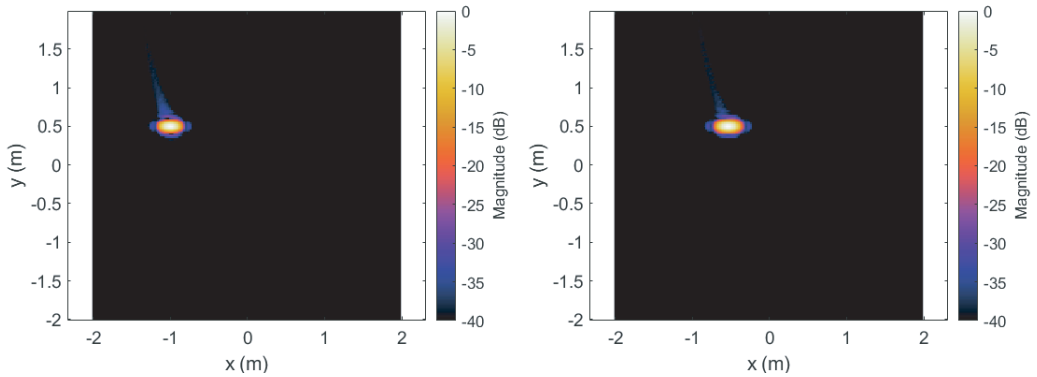

Figure 5. Image of point target at $(x_o, y_o, z_o) = (-1, 0.5, 1.5)$ m created using a linear aperture with the image formation plane set to (a) $z = 1.5$ m and (b) $z = 0$ m.

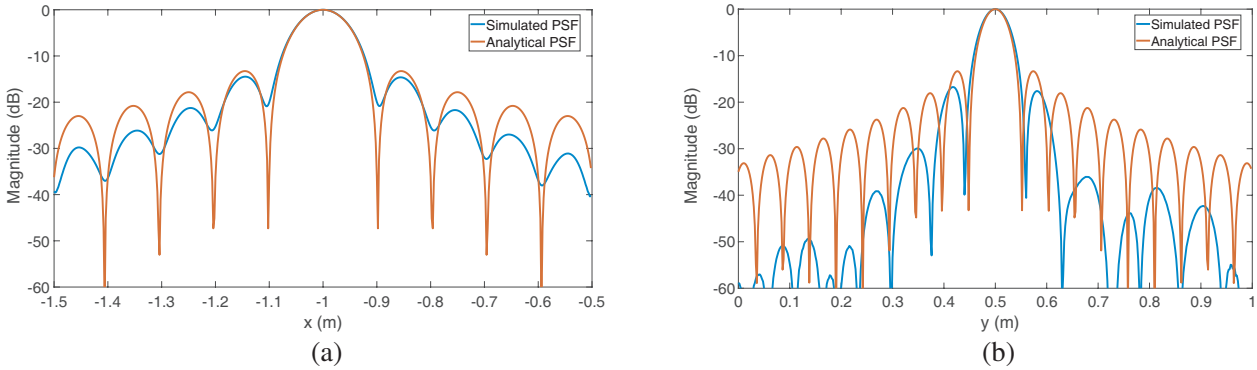

Figure 6. Comparison plots of the simulated and analytic PSFs for the linear aperture in the (a) x and (b) y directions over the target peak.

$\delta_y = 0.051$ m. 1-D slices of the image created at $z = 1.5$ m are shown in the x and y dimensions below. These slices are compared with the formulas in Eq. (8). From Fig. 6 it is clear that the analytic PSF follows the simulation closely. The simulated resolution in the x-direction was 0.104 m, which is a slight deviation from the derived resolution. In the y-direction, the simulated resolution is 0.06 m, which is 4 mm larger than the analytical resolution. The main difference between the simulated and analytical PSFs is the side-lobe structure further away from the peak. This is most likely due to the fact that the assumptions used in the derivation break down as angles are increased. However, these differences in side-lobe magnitude do not detract from the quality of the PSF analysis. The resolution formulas derived for an image formed in the xy-plane using a linear aperture are adequately accurate for the purpose of determining the properties of an image given a set of radar parameters.

The derived PSF for a vertical grid is compared with simulated data. Fig. 7 shows images formed in horizontal planes placed at $z = 1.5$ m and $z = 0$ m for the vertical grid aperture and target shown in Fig. 4. These images were formed using a hanning window in both the range and aperture dimensions. The dynamic range is increased from 40 dB to 50 dB so that the artifacts in the ground plane image are visible. The target is only present in the image formed at 1.5 m, which is the height of the target. Vertical resolution has removed the ambiguity between those two images. The image formed at the ground plane shows sidelobes from the target PSF. The strongest response of these sidelobes is about 35 dB weaker than the peak of the target response.

Next, the resolution of the analytic PSF is compared with that of the simulated PSF. According to Eq. (17), the resolution in the x, y, and z directions are respectively given as $\delta_x = 0.101$ m, $\delta_y = 0.051$ m,

and $\delta_z = 0.185\,\text{m}$. Amplitude values through the center of the target are shown in the x, y, and z directions for both the analytical and simulated PSF in Fig. 8. In both the x and y-directions, the simulated PSFs showed the same results as in the case of the linear aperture. In the z-direction, the simulated PSF had a resolution of 0.198 m, which is 7 mm coarser than that of the analytical PSF. Thus, in the vertical dimension, the analytical expression is also valid.

These PSF simulations agree well with the derived analytical expressions derived in Section 2 despite the approximations applied in those derivations. This is particularly true with regard to the PSF's mainlobe, which determines the imaging system's resolution. The resolution is the most important performance metric of the imaging system, indicating the system's ability to accurately represent the scene under interrogation.

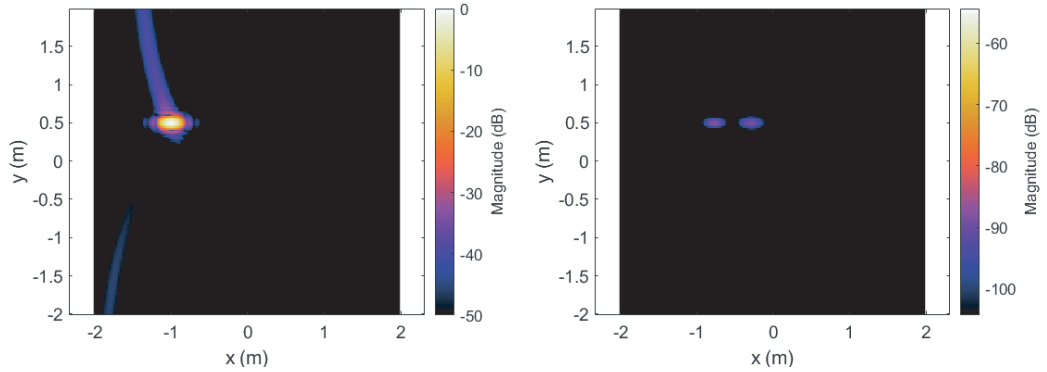

Figure 7. Image of point target at $(x_o, y_o, z_o) = (-1, 0.5, 1.5)\,\text{m}$ created using a vertical grid aperture with the image formation plane set to (a) $z = 1.5\,\text{m}$ and (b) $z = 0\,\text{m}$.

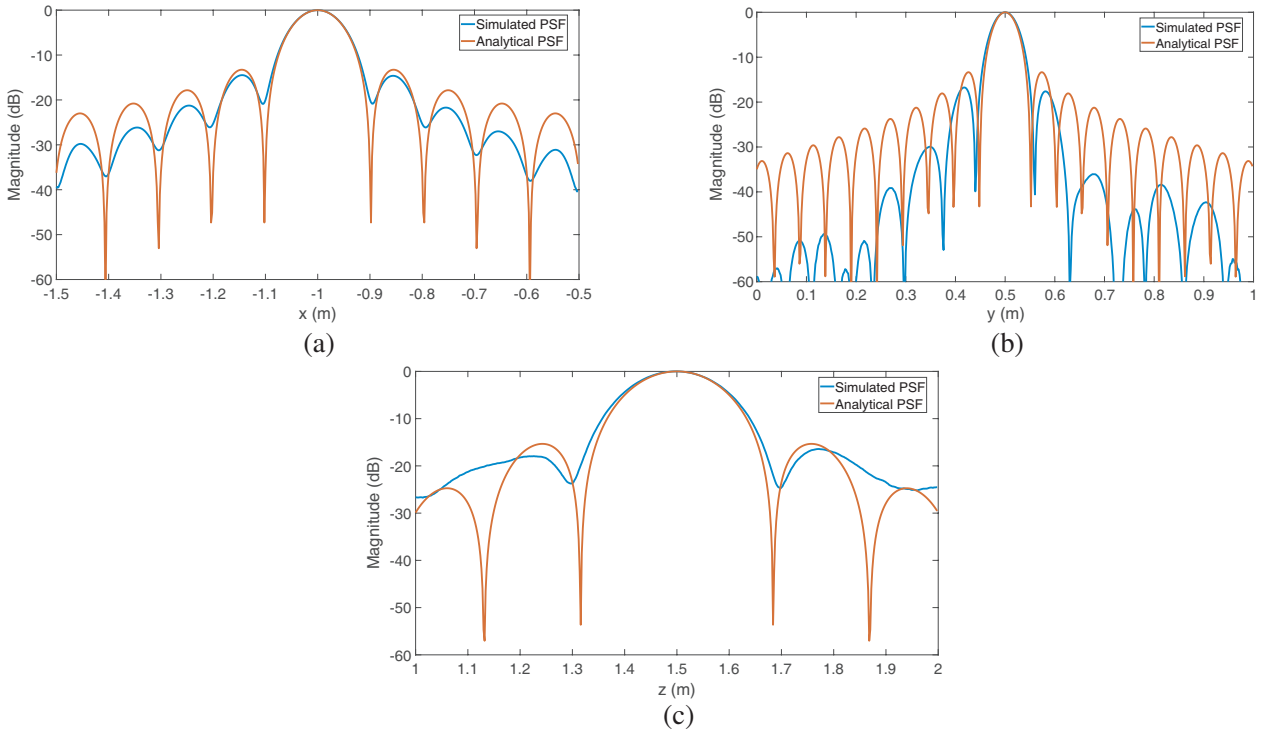

Figure 8. Comparison plots of the simulated and analytic PSFs for the linear aperture in the (a) x and (b) y directions over the target peak.

4. EXPERIMENTAL RESULTS

In this section, the concept of vertical resolution is investigated further using measured radar data. A radar was placed on a linear scanning system, shown in Fig. 9(b). This consists of both a horizontal and vertical linear scanner, which is able to step through positions to generate a desired aperture.

The observed test scene is shown in Fig. 9(a). Two surrogate metal landmines, with a diameter of 13.16 in. and a height of 3.54 in., are used. The landmines are placed 4 m in ground range from the scanner axis. They are labeled Target 1 and Target 2, with Target 1 placed at a height of 1.4 m and Target 2 at a height of 0.7 m. This experiment is designed to demonstrate the resolution afforded by the vertical grid aperture. Furthermore, it is used to demonstrate the importance of vertical resolution in imaging objects above the ground.

(a) (b)

Figure 9. (a) Two landmines stacked vertically using styrofoam blocks. (b) Scanner on ARL facility capable of both vertical and horizontal scanning.

The radar used to collect the data is a Xilinx RF system-on-a-chip paired with a custom RF front end. The operating band of this system is 2.2 GHz to 3.7 GHz. A stepped-frequency waveform with a 1.5-MHz frequency step size is used. The grid aperture was sampled with an along track spacing of 0.006 m and a vertical spacing of 0.05 m. The across-track position of the scanner remains at 0 m.

The two apertures are shown in Fig. 10. In the first experiment data was collected with a linear aperture at a height of 2 m. Since the linear aperture does not achieve vertical resolution, the imagery is formed in the ground plane. Data collected with a vertical grid aperture has vertical resolution. Thus, a 3-D image can be created. Imagery is shown as slices through the 3-D volume.

The ground plane image created using the linear aperture is shown in Fig. 11. Energy from objects at all heights are projected onto the ground plane. Thus, even though these two targets are at different heights, it is difficult to distinguish them from one another in the ground plane image. Furthermore, all clutter in the surrounding environment that may be at different heights is projected into this area.

The images of the targets obtained with the 3-D imaging system, in horizontal planes at at $z = 0.7$ m and $z = 1.4$ m, are shown in Fig. 12.

The ability to detect targets in these images can be determined using SCR. This ratio is defined as the ratio of the peak of the target to the mean of the pixel/voxel power. Table 1 shows a list of SCR values for both of the landmine targets from the images created using the linear aperture and vertical grid aperture. A circle of radius 0.3 m is used to remove the landmine from the calculation of the mean clutter power. For the linear aperture, the image was created in the ground plane, so the target and clutter values were taken from the same image for both Target 1 and Target 2. In general, the images generated using the vertical grid apertures had much better SCRs, resulting from to the spatial separation of the clutter. The SCR improvement using a grid aperture was 10.79 dB for target 1 and 11.87 dB for target 2. Part of why the SCR was smaller when using a linear aperture was because Target 1 was included in the clutter mean for the SCR calculation for Target 2, and vice-versa. Spatially

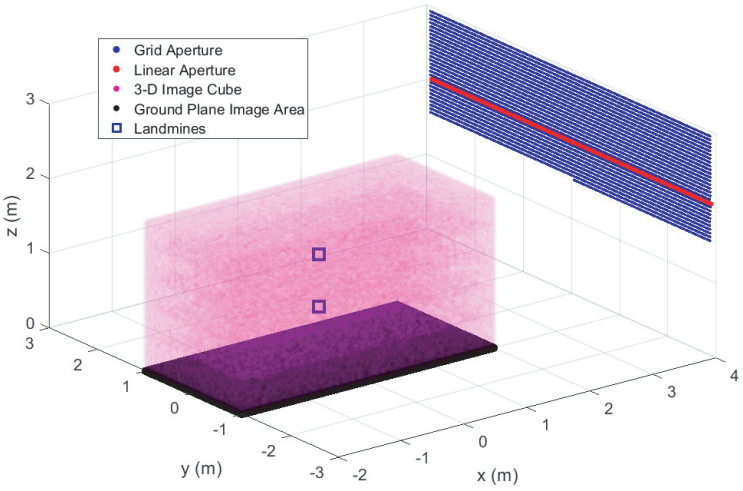

Figure 10. Linear aperture, two landmines, and the image area.

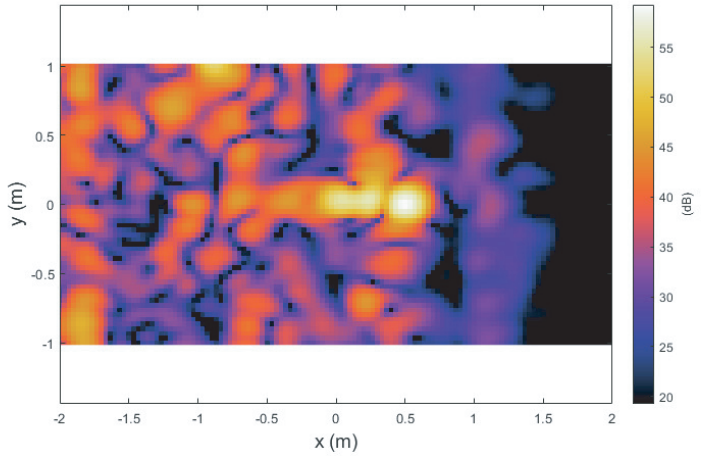

Figure 11. Ground plane image of the test scene using data collected with a linear aperture.

Table 1. SCR in imagery created using grid aperture and linear aperture.

Target	Aperture	Peak (dB)	Mean (dB)	SCR (dB)
Target 1	Linear	59.27	34.29	24.98
Target 2	Linear	55.93	34.25	24.68
Target 1	Grid	59.84	24.07	35.77
Target 2	Grid	55.71	22.15	33.55

separating these targets would greatly improve the SCR.

Figure 13 shows a comparison between experimental and modeling data for a yz-slice of the image created using a vertical grid at the cross-range position containing the targets. A model was created using the same geometry and set of frequencies using the ARL finite-difference time-domain (AFDTD) electromagnetic modeling software [26]. A simplified landmine model was used to represent the target scene. There is excellent agreement between the images created by the measured data and the modeled

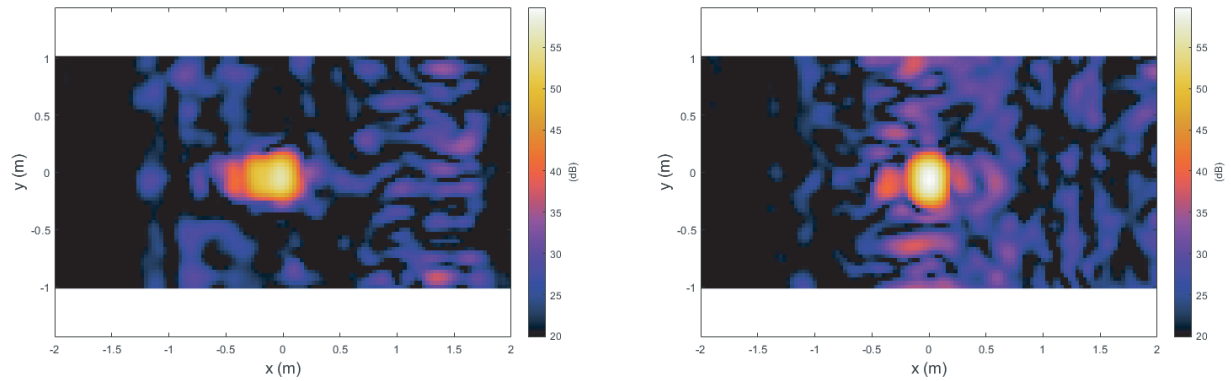

Figure 12. Horizontal slices of 3-D image containing vertically displaced landmines at (a) $z = 0.7\,\text{m}$ and (b) $z = 1.4\,\text{m}$.

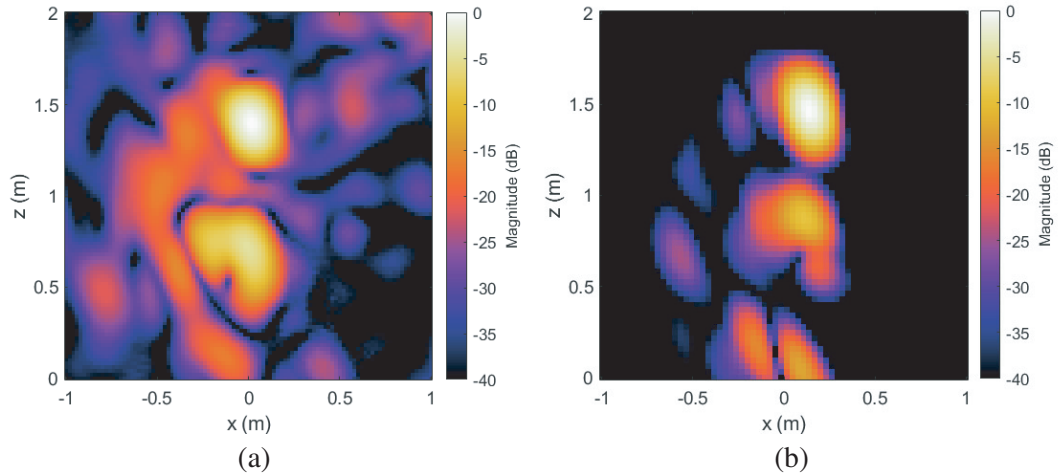

Figure 13. Comparison of imagery in an across-track-vertical slice of the 3-D image at the along track position of the landmine targets between (a) experimental data and (b) modeling data.

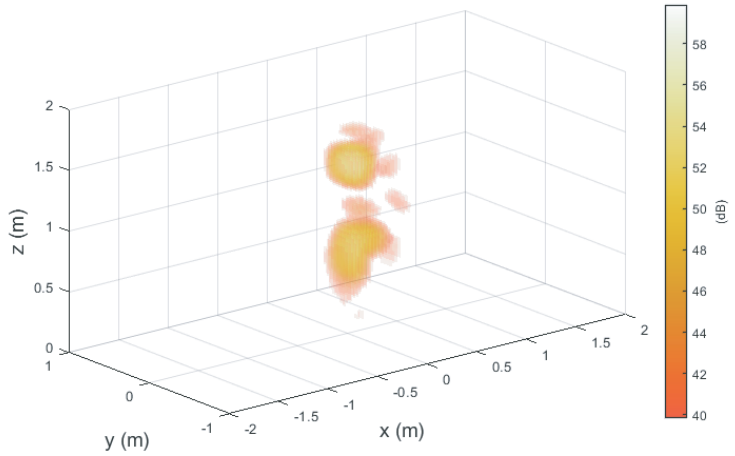

Figure 14. 3-D image of landmines.

data. This shows that most of the artifacts present in the experimental image are signals and sidelobes created by the targets themselves, rather than artifacts from clutter or the imaging procedure.

Finally, a 3-D image, shown in Fig. 14, is created using the 3-D data volume from the grid aperture data. The data is rendered by varying the opacity of the image proportionally with the voxel strength. The strongest voxels are the most opaque, and the weakest voxels are transparent. A 20 dB dynamic range is used for this representation so that the targets are displayed clearly; however, with this representation the two targets are easily identified and localized in 3-D space.

5. CONCLUSION

In this paper, we presented a possible approach for achieving 3-D resolution in radar images, with the goal of improving the detectability of obscured targets by reducing the amount of clutter in the target image plane. The underlying principle relies on spreading the clutter energy over a large 3-D volume of space, as compared to concentrating it over a single plane, as in traditional 2-D SAR imaging. Since the target is correctly focused in a small number of resolution cells in the 3-D space, the SCR metric is improved.

The SAR system considered in this investigation operates in the near field over a wide frequency band and a wide integration angle. In Section 2, we made some simplifying assumptions in order to derive analytic expressions for the PSF and the systems resolution in the three directions. These approximations were validated in Section 3 by direct computer simulations using a point target, as far as the PSF mainlobe is concerned. In Section 4, experimental data using a radar scanner demonstrated the ability to generate 3-D imagery with adequate vertical resolution. A comparison between the images generated by employing a linear aperture and a 2-D vertical-grid aperture showed a clear SCR improvement in the latter configuration. Furthermore, correct target localization was achieved in the 3-D images.

The experimental setup included two large scattering objects placed in a laboratory environment. However, this concept can be applied to any discrete or distributed clutter objects located in the target vicinity. By resolving the energy from these clutter objects in the 3-D space, the peak and mean clutter powers are reduced throughout the image, with beneficial effects on target detectability.

Future work will seek to apply this concept to obscured targets in more practical sensing scenarios. The follow-on experiments will be conducted from a flying UAV platform carrying the radar system, in a realistic environment. For such implementation, a major issue with the 2-D vertical aperture obtained via raster scan is the very large number of spatial samples needed to satisfy the usual sampling requirements. Additionally, a back-and-forth flight path for the platform is undesirable due to the slow coverage rate. Therefore, a significant part of the future study will be dedicated to optimizing the flight path and sampling scheme without reducing the grating lobe separation in the image. An alternate approach would involve applying multiple-input-multiple-output concepts to create an effective aperture using multiple platforms that satisfies both resolution and sampling requirements. Finally, limitations such as flight time and SWAP will be tested in real environments to determine the viability of these concepts.

ACKNOWLEDGMENT

This research was supported by the U.S. Army Combat Capabilities Development Command Army Research Laboratory (CCDC ARL). We would like to thank Kenneth Ranney of the U.S. Army CCDC ARL for his contributions to this research.

REFERENCES

1. Dogaru, T. V., B. R. Phelan, and C. D. Kelly, "Analysis of buried target and clutter signature in ground penetrating radar imaging," *Proc. SPIE 12108, Radar Sensor Technology XXVI*, Vol. 12108, 1210804, Orlando, FL, USA, SPIE, Bellingham, WA, April 3–7, 2022.

2. Bradley, M. R., T. R. Witten, R. McCummins, M. Crowe, S. Stewart, and M. Duncan, "Mine detection with a multichannel stepped-frequency ground-penetrating radar," *Proc. SPIE 3710, Detection and Remediation Technologies for Mines and Minelike Targets IV*, Vol. 3710, 953–960, Orlando, FL, USA, SPIE, Bellingham, WA, April 5–9, 1999.
3. Bradley, M. R., T. R. Witten, R. McCummins, M. Duncan, M. Crowe, and S. Stewart, "Mine detection with a ground-penetrating synthetic aperture radar," *Proc. SPIE 4038, Detection and Remediation Technologies for Mines and Minelike Targets V*, Vol. 4038, 1001–1007, Orlando, FL, USA, SPIE, Bellingham, WA, April 24–28, 2000.
4. Bradley, M. R., T. R. Witten, R. McCummins, and M. Duncan, "Mine detection with ground penetrating synthetic aperture radar," *Proc. SPIE 4742, Detection and Remediation Technologies for Mines and Minelike Targets VII*, Vol. 4742, 248–258, Orlando, FL, USA, SPIE, Bellingham, WA, April 1–5, 2002.
5. Chambers, D. H., D. W. Paglieroni, J. E. Mast, and N. R. Beer, "Real-time vehicle-mounted multistatic ground penetrating radar imaging system for buried object detection," Report LLNL-TR-615452, Lawrence Livermore National Laboratories, USA, January 2013.
6. Paglieroni, D. W., D. H. Chambers, J. E. Mast, S. W. Bond, and N. R. Beer, "Imaging modes for ground penetrating radar and their relation to detection performance," *IEEE Journal of Selected Topics in Applied Earth Observations and Remote Sensing*, Vol. 8, No. 3, 1132–1144, 2015.
7. Kositsky, J. and P. Milanfar, "Forward-looking high-resolution GPR system," *Proc. SPIE 3710, Detection and Remediation Technologies for Mines and Minelike Targets IV*, Vol. 3710, 1052–1062, Orlando, FL, USA, SPIE, Bellingham, WA, April 5–9, 1999.
8. Kositsky J. and C. A. Amazeen, "Results from a forward-looking GPR mine detection system," *Proc. SPIE 4394, Detection and Remediation Technologies for Mines and Minelike Targets VI*, Vol. 4394, 700–711, Orlando, FL, USA, SPIE, Bellingham, WA, April 16–20, 2001.
9. Bradley, M. R., T. R. Witten, M. Duncan, and R. McCummins, "Mine detection with a forward-looking ground-penetrating synthetic aperture radar," *Proc. SPIE 5089, Detection and Remediation Technologies for Mines and Minelike Targets VIII*, Vol. 5089, 334–347, Orlando, FL, USA, SPIE, Bellingham, WA, April 21–25, 2003.
10. Bradley, M. R., T. R. Witten, M. Duncan, and R. McCummins, "Anti-tank and side-attack mine detection with a forward-looking GPR," *Proc. SPIE 5415, Detection and Remediation Technologies for Mines and Minelike Targets IX*, Vol. 5415, 421–432, Orlando, FL, USA, SPIE, Bellingham, WA, April 12–16, 2004.
11. Ressler, M., L. Nguyen, F. Koenig, D. Wong, and G. Smith, "The Army Research Laboratory (ARL) synchronous impulse reconstruction (SIRE) forward-looking radar," *Proc. SPIE 6561, Unmanned Systems Technology IX*, Vol. 6561, Article id. 656105, Orlando, FL, USA, SPIE, Bellingham, WA, April 9–13, 2007.
12. Phelan, B. R., K. I. Ranney, K. A. Gallagher, J. T. Clark, K. D. Sherbondy, and R. M. Narayanan, "Design of ultrawideband stepped-frequency radar for imaging of obscured targets," *IEEE Sensors Journal*, Vol. 17, No. 14, 4435–4446, 2017.
13. Ulander, L. M. H., et al., "Analysis of CARABAS VHF SAR data from BALTASAR-96," *IGARSS'97. 1997 IEEE International Geoscience and Remote Sensing Symposium Proceedings. Remote Sensing — A Scientific Vision for Sustainable Development*, Vol. 2, 797–799, Singapore, IEEE, Piscataway, NJ, August 3–8, 1997.
14. Gasson, J., D. Hughes, M. Poulter, and G. Crisp, "Development of an ultra wide-band SAR for minefield detection," *IEEE 1999 International Geoscience and Remote Sensing Symposium. IGARSS'99 (Cat. No.99CH36293)*, Vol. 5, 2474–2476, Hamburg, Germany, IEEE, Piscataway, NJ, June 28–July 2, 1999.
15. Aubry, W. M., et al., "Airborne sensor concept to image shallow-buried targets," *Proceedings of the 2002 IEEE Radar Conference (IEEE Cat. No.02CH37322)*, 233–236, Long Beach, CA, USA, IEEE, Piscataway, NJ, April 25, 2002.

16. Le Goff, M., R. Guillerey, F. Gallais, J. Andrieu, B. Beillard, and B. Jecko, "Ultra wide band synthetic aperture radar for the detection of mined areas," *RADAR 2002*, 526–530, Edinburgh, UK, IEEE, Piscataway, NJ, October 15–17, 2002.
17. Schleijpen, H. M. A., "Landmine detection technology research programme at TNO," *Proceedings of the 2nd International Workshop on Advanced Ground Penetrating Radar, 2003*, 138–143, Delft, Netherlands, IEEE, Piscataway, NJ, May 14–16, 2003.
18. Moussally, G., K. Breiter, and J. Rolig, "Wide-area landmine survey and detection system," *Proceedings of the Tenth International Conference on Grounds Penetrating Radar, 2004. GPR 2004*, 693–696, Delft, Netherlands, IEEE, Piscataway, NJ, June 21–24, 2004.
19. Fasano, G., A. Renga, A. R. Vetrella, G. Ludeno, I. Catapano, and F. Soldovieri, "Proof of concept of micro-UAV-based radar imaging," *2017 International Conference on Unmanned Aircraft Systems (ICUAS)*, 1316–1323, Miami, FL, USA, IEEE, Piscataway, NJ, June 13–16, 2017.
20. García Fernández, M., et al., "Synthetic aperture radar imaging system for landmine detection using a ground penetrating radar on board a unmanned aerial vehicle," *IEEE Access*, Vol. 6, 45100–45112, 2018.
21. García Fernández, M., Y. Á. López, and F. L. Andreés, "Airborne multi-channel ground penetrating radar for improvised explosive devices and landmine detection," *IEEE Access*, Vol. 8, 165927–165943, 2020.
22. Schartel, M., R. Burr, W. Mayer, N. Docci, and C. Waldschmidt, "UAV-based ground penetrating synthetic aperture radar," *2018 IEEE MTT-S International Conference on Microwaves for Intelligent Mobility (ICMIM)*, 1–4, Munich, Germany, IEEE, Piscataway, NJ, April 15–17, 2018.
23. Dill, S., E. Schreiber, M. Engel, A. Heinzel, and M. Peichl, "A drone carried multichannel synthetic aperture radar for advanced buried object detection," *2019 IEEE Radar Conference (RadarConf)*, 1–6, Boston, MA, USA, IEEE, Piscataway, NJ, April 22–26, 2019.
24. Richards, M. A., *Principles of Modern Radar, Vol 1: Basic Principles*, SciTech Publishing, Inc., Raleigh, NC, USA, 2010.
25. Dogaru, T. V., "Performance analysis of side-looking ground penetrating radar imaging," Report ARL-TR-9388, Army Research Laboratory, USA, January 2022.
26. Dogaru, T., "AFDTD user's manual," Report ARL-TR-5145, Army Research Laboratory, USA, March 2010.